Journal of Materials Chemistry A

ROYAL SOCIETY OF CHEMISTRY

PAPER

View Article Online
View Journal

Cite this: DOI: 10.1039/d5ta10141g

The impact of dendrites and related compositional fluctuations on hydrogen absorption thermodynamics in bcc multi-principal element alloys

Veronica Enblom,[a] Fernando Maccari,[b] Franziska Scheibel,[b] Aaron Keith,[cd] Vitalie Stavila,[e] Claudia Zlotea,[c] Oliver Gutfleisch,[b] Paul F. Henry[af] and Martin Sahlberg*[a]

Solid-state hydrogen storage is a key concept in the prospect of a sustainable hydrogen economy. Multi-principal element alloys (MPEAs) with a body-centred cubic (bcc) structure are promising hydride-forming materials, but often solidify with dendritic, compositionally segregated microstructures. This study examines how such compositional fluctuations affect hydride formation thermodynamics, using the $Ti_{30}V_{30}Cr_{24}Nb_{16}$ MPEA as an exemplar. Dendritic segregation was controlled by varying the solidification rate and eliminated through high-temperature solid-solution annealing. Rapid solidification by melt-spinning successfully suppressed dendrites but resulted in an alloy that did not absorb hydrogen, and <2 wt% of a TiO-type oxide finely dispersed throughout the material. In contrast, the annealed alloy exhibited full hydrogen uptake (3.3 wt%) and a flatter monohydride-dihydride transition plateau in the pressure-composition isotherms compared with the dendritic as-cast alloy. Despite these compositional fluctuations, the derived thermodynamic parameters (ΔH and ΔS) were indistinguishable within experimental uncertainty. Our experiments reveal that the compositional fluctuations caused by the dendrite formation influence the slope of the equilibrium plateau pressures, while the overall composition dominates the fundamental thermodynamic properties.

Received 11th December 2025
Accepted 7th May 2026

DOI: 10.1039/d5ta10141g

rsc.li/materials-a

1 Introduction

Solid-state hydrogen storage remains a key enabler for a safe and efficient hydrogen economy. Metal hydrides provide a practical route by allowing hydrogen atoms to occupy interstitial sites within metals and alloys, offering safe storage with volumetric energy densities often exceeding that of liquid hydrogen (8 MJ L^{-1}).[1] Among hydride-forming systems, multi-principal element alloys (MPEAs) are currently attracting significant attention because their compositional diversity allows the combination of strong and weak hydrogen-binding elements, enabling a balance between hydrogen uptake and release.[2] Body-centred cubic (bcc) MPEAs are particularly attractive since they can reversibly absorb up to 2 H/M, achieving practical gravimetric capacities above the benchmark $LaNi_5$ (2.0–3.5 *vs.* 1.5 wt% H) while maintaining faster kinetics and better cycling stability than higher-capacity systems such as Mg-based hydrides.[2–5]

These alloys generally absorb hydrogen in a two-step reaction near ambient temperature: first forming a monohydride from a dilute solid solution, then a dihydride.[6,7] These reactions are both first-order transitions, giving rise to pressure plateaus in the pressure-composition isotherms (PCIs) that correspond to two-phase coexistence.[6,8] The stability of each hydride phase – *i.e.*, its temperature and pressure-dependence – is governed by the composition-dependent hydride formation enthalpy (ΔH), which can be extracted from the equilibrium plateau pressure using van't Hoff analysis.[9] Comparing ΔH values across alloys and interpolating between known systems enables the prediction and design of new alloys with targeted thermodynamic properties.[10]

However, this approach implicitly assumes that ΔH of hydrogenation is independent of microstructure – an assumption recently challenged by Rong *et al.*,[11] who reported a 4% smaller (less exothermic) ΔH for annealed compared to as-cast

[a]*Department of Chemistry – Ångström Laboratory, Uppsala University, Box 538, 751 21 Uppsala, Sweden. E-mail: martin.sahlberg@kemi.uu.se*
[b]*Functional Materials, Institute of Material Science, Technical University of Darmstadt, 64287 Darmstadt, Germany*
[c]*Université Paris-Est Créteil, CNRS, ICMPE, UMR 7182, 2 rue Henri Dunant, Thiais 94320, France*
[d]*School of Engineering and Materials Science, Queen Mary University of London, Mile End Campus, London E1 4NS, UK*
[e]*Sandia National Laboratories, Livermore, California 94551, USA*
[f]*ISIS Pulsed Neutron & Muon Facility, Rutherford Appleton Laboratory, Harwell Campus, Didcot OX11 0QX, UK*

$Ti_{20}V_{68}Cr_{12}$. The difference was attributed to reduced elemental segregation after annealing, which also produced a flatter plateau. This agrees with the established understanding that chemical heterogeneity broadens the distribution of interstitial site energies and produces sloped plateau pressures,[12,13] as further illustrated by the sensitivity of equilibrium pressure to composition. For instance, increasing the Cr content by 5 at%, from $(TiVNb)_{70}Cr_{30}$ to $(TiVNb)_{65}Cr_{35}$, raises the equilibrium pressure at 70 °C by 225% (from 3.4 to 11.1 bar).[14] Because plateau sloping reflects variations in local chemical potential, it follows that changes in the degree of segregation – and thus microstructure – can influence the apparent ΔH. Such microstructure dependence complicates the comparison of thermodynamic data across alloys and hinders reliable prediction of equilibrium pressures, posing particular challenges for bcc-structured MPEAs where microstructural control is inherently difficult.

Controlling microstructure in bcc MPEAs is challenging since the bcc phase is often metastable at ambient temperatures and stable as a single phase only at very high temperatures (typically 1200 °C).[15–17] Below this temperature, Laves phases readily form, limiting the heat-treatment window for homogenisation.[15] Moreover, most bcc MPEAs solidify with dendritic microstructures[15,18] – *i.e.*, microscale elemental segregation (or microsegregation) resembling a continuum of bcc phases – which produces sloping, non-ideal pressure plateaus. This heterogeneity stems from constitutional undercooling, partially driven by a positive enthalpy of mixing or large differences in elemental melting points.[19] Consequently, dendrite cores tend to be enriched in high-melting-point elements, leaving the interdendritic regions depleted. While this segregation can be suppressed if the cooling rate outpaces diffusion, or eliminated *via* high-temperature homogenisation, both approaches are experimentally challenging.[15] As a result, as-cast dendritic MPEAs are frequently used in studies under the assumption that the microstructure has no impact on thermodynamic properties.

This study investigates the potential microstructure dependence of the thermodynamic parameters (ΔH and ΔS) for hydride formation in the MPEA $Ti_{30}V_{30}Cr_{24}Nb_{16}$. The Ti–V–Cr–Nb system was selected due to its extensive prior study,[14,20–26] and promising room-temperature cycleability.[20] The specific composition was chosen to target a broad single-phase region near equimolar composition to facilitate homogenisation. Dendrite suppression and removal, without secondary phase formation, were achieved through rapid solidification *via* melt-spinning and high-temperature homogenisation, respectively. The resulting samples were characterised using PCIs and van't Hoff analysis to evaluate their hydride formation behaviour.

2 Experimental

2.1 CALPHAD predictions

To identify a composition suitable for microstructural homogenisation, CALPHAD calculations were performed on a series of alloys based on the equimolar TiVCrNb system. The equimolar composition is predicted to exhibit a single-phase bcc structure at elevated temperatures.[14,23] However, CALPHAD models also predicted the formation of secondary phases at intermediate temperatures, which should be avoided – a C15 Laves phase below ≈900 °C and an additional bcc phase below ≈700 °C. The Laves phase is likely of the type Nb(Ti, V)Cr_2,[27] where suppression is expected by reducing either the Nb or Cr content. Cr plays a key role in hydride destabilisation[14,23] and oxidation resistance,[15] favourable properties for retention in a candidate MPEA. Taking these factors into consideration to enable controlled comparison between dendritic and homogenised samples, the composition series explored here focused on reducing Nb in favour of Ti and V. Phase stability was evaluated using Thermo-Calc (version 2022a) with the TCHEA3 database.[28] Based on these predictions, the composition $Ti_{30}V_{30}Cr_{24}Nb_{16}$ was selected for synthesis and further investigation.

2.2 Synthesis

$Ti_{30}V_{30}Cr_{24}Nb_{16}$ alloys were synthesised by vacuum arc melting of stoichiometric elemental mixtures. Ti (2–5 mm pieces, 99.995%), V (<3 mm granules, 99.9%), and Nb (3 × 3 mm pellets, 99.95%) were sourced from ChemPur, while Cr (2–5 mm cuttings, 99.95%) was obtained from a recycled sputtering target (Kurt J. Lesker). Melting was performed on a water-cooled copper hearth in a custom-built arc-melting setup. Two high-purity Ti ingots were used as getters to remove residual oxygen, nitrogen, and hydrogen. Each 5 g alloy ingot was re-melted at least five times and flipped between melts to promote compositional homogeneity.

Following synthesis, the ingots were processed through three different routes to obtain distinct microstructures. One ingot was kept in the as-cast state, mounted in bakelite, and sectioned both vertically and horizontally (3 mm thick cross-sections) using a Buehler IsoMet High Speed Pro precision cutter for microstructural and phase analysis. Two ingots were re-melted and suction-cast into a cylindrical water-cooled copper mould (5 mm diameter, 30 mm length) using a Bühler MAM-1 arc melter. Suction casting was used to promote more uniform solidification along the length of the rod, minimising the grain size gradients and microstructural variations typically observed in arc-melted ingots.[29] The cast rods were sectioned into 3 mm thick discs for microstructural characterisation, X-ray diffraction (XRD), and hydrogen absorption measurements. Two ingots were re-melted by induction melting under argon atmosphere in a boron nitride crucible and rapidly solidified *via* melt spinning (Bühler Melt Spinner). The melt was ejected through a 2 mm diameter nozzle under 400 mbar argon overpressure onto a water-cooled copper wheel rotating at 40 m s^{-1} surface velocity. The resulting ribbons were approximately 5 mm wide and 50 μm thick.

2.3 Annealing treatments

Annealing was performed on suction-cast samples to eliminate dendritic elemental segregation through solid solution treatment at 1000 °C and 1400 °C, both within the CALPHAD-predicted single-phase bcc region. The 1000 °C annealing was conducted in a muffle furnace, with samples wrapped in

tantalum foil and sealed in evacuated quartz ampoules to prevent oxidation. The tantalum foil served both as an oxygen and nitrogen getter and as a barrier to prevent the alloy from reacting with the quartz, forming silicides. Heating was performed at 20 °C min^{-1} up to 1000 °C, followed by a 14-day isothermal hold to reach thermodynamic equilibrium. The samples were subsequently quenched in water.

Annealing at 1400 °C was carried out in a vertical tube furnace (MTI GSL-1700X) under constant argon flow. Samples were wrapped in tantalum foil and placed inside alumina crucibles suspended in the furnace chamber by a metal thread attached to an electromagnetic release system. The chamber was evacuated and flushed three times with argon before establishing a continuous flow. Heating was ramped at 10 °C min^{-1} to 1200 °C, then 5 °C min^{-1} to 1400 °C. The crucibles were drop-quenched into paraffin oil after a 1 h isothermal hold.

All annealed samples exhibited a clean metallic surface, indicating minimal oxidation. Subsequent EDS analysis did not detect tantalum, suggesting no diffusion into the samples. Samples were cleaned by sonication in deionised water, acetone, and ethanol before subsequent analysis.

2.4 Microstructural characterisation

Microstructural characterisation was performed to evaluate phase distribution, grain morphology, and elemental homogeneity across differently processed samples, using scanning electron microscopy (SEM) and energy-dispersive spectroscopy (EDS).

Cross-sections of the arc-melted, suction-cast, and melt-spun samples – as well as annealed suction-cast samples – were prepared for analysis. Samples were hot-mounted in conductive bakelite (PolyFast, Struers). The melt-spun ribbon was mounted standing upright to allow observation through its thickness and along the solidification direction. All samples were ground and polished using standard metallographic procedures, followed by chemical polishing with colloidal silica (OP–S, Struers; 40 nm particle size) mixed with 10 vol% ammonia (25%, VWR Chemicals) and 10 vol% hydrogen peroxide (30%, Merck). Samples were then cleaned by sonication in acetone and ethanol, etched using Kroll's reagent, and finally re-cleaned in deionised water, acetone, and ethanol. An unmounted melt-spun ribbon was also examined in as-processed condition for surface/topography characterisation.

Microstructural analysis was carried out using a Carl Zeiss Merlin field-emission scanning electron microscope (FE-SEM) equipped with an Oxford Instruments X-Max 80 mm^2 silicon drift detector for EDS. SEM imaging was performed using secondary electron (SE) and backscattered electron (BSE) detection. EDS spectra and mapping were acquired at an accelerating voltage of 10 kV, beam current of 2 nA, and a working distance of 8.5 mm, using the Aztec software (version 6.1, Oxford Instruments). The K-lines were used for quantification of Ti, V, and Cr, and the L-lines for Nb.

2.5 Phase analysis with X-ray and neutron diffraction

X-ray diffraction (XRD) was performed to determine the phase purity and lattice parameters of samples prepared under different processing conditions. Measurements were carried out in Bragg–Brentano geometry on the same polished cross-sections used for microstructural characterisation. Data were collected using a Bruker D8 Advance diffractometer equipped with a LynxEye XE position-sensitive detector and Cu Kα radiation ($\lambda = 1.5418$ Å), over a 2θ range of 5–120° with a step size of 0.019°.

Neutron diffraction was performed on the dendrite-free samples – namely the annealed suction-cast and melt-spun alloys – using the POLARIS diffractometer at the ISIS Neutron and Muon Source, Rutherford Appleton Laboratory, United Kingdom,[30] to quantify oxide phase fractions. Neutron diffraction probes the bulk of the material and thus ensures representative, average phase fractions. Although only minor oxide fractions were present, their detection was facilitated by the strong scattering contrast between oxygen ($b = 5.803$ fm) and the alloy, which has a near-zero average coherent scattering length ($\bar{b} = 0.855$ fm for $Ti_{30}V_{30}Cr_{24}Nb_{16}$). The corresponding datasets are available at ref. 31 and 32.

Both the XRD and neutron diffraction data were fitted using TOPAS Academic (version 6).[33] Due to the strong crystallographic texture observed in several samples, Pawley fitting was used for phase identification and lattice parameter refinement for the in-house XRD data, while full Rietveld refinement was performed to obtain phase fractions from the neutron data. The lattice parameters for the as-cast suction-cast sample, refined from XRD, were subsequently used to calculate hydrogen concentrations during absorption measurements.

2.6 Hydrogen absorption measurements

Hydrogen absorption measurements were conducted on as-cast dendritic and annealed dendrite-free suction-cast samples using a Sievert-type apparatus equipped with a manually operated manometric system and thermostatically calibrated volumes. Approximately 350 mg of each sample was loaded into the reactor and activated by heating to 410 °C under dynamic vacuum ($\approx 10^{-7}$ mbar) for 3 h, followed by exposure to 54 bar of hydrogen gas at 25 °C. The pressure was chosen based on equilibrium data reported for similar compounds[23] to ensure complete hydrogenation. Hydrogen was desorbed at 410 °C for 4 h under dynamic vacuum prior to the thermodynamic measurements.

Pressure-composition isotherms (PCIs) were acquired at 105 °C, 130 °C, and 155 °C by introducing incremental hydrogen doses and allowing the system to reach equilibrium at each step. Equilibrium was assumed when the pressure change was less than 1 mbar per 10 minutes. Between isotherms, desorption was carried out under the same conditions used after activation. The hydrogen content was calculated using the real gas equation *via* the GASPAK Excel add-in (version 3.32, Horizon Technologies). The dead volume was corrected by subtracting the calculated sample volume from the empty sample holder volume (1.68 cm^3). The sample volume was derived from the experimental masses (345.9 and 356.6 mg for the dendritic and homogenised samples, respectively) and the

theoretical density (6.257 g cm^{-3}), calculated using the unit cell edge $a = 3.116$ Å.

Plateau slopes were determined by fitting the linear region of the plateaus and using the corresponding first derivatives to quantify their gradients. The hydride formation enthalpy (ΔH) and entropy (ΔS) were obtained from van't Hoff analysis of the equilibrium plateau pressures. To ensure consistency and comparability, the same equilibrium pressure extraction point was used across all samples and temperatures, in accordance with best practice recommendations.[34] The extraction point H/M = 1.1, corresponding to the midpoint of the plateau at 155 °C, was used for the primary comparison between samples. Additional analyses were performed using H/M = 0.9 and 1.3 to evaluate the sensitivity of the calculated ΔH and ΔS values to the extraction point.

3 Results

3.1 CALPHAD-based composition selection

Phase stability in the Ti–V–Cr–Nb system was assessed by CALPHAD calculations to identify compositions exhibiting a wide single-phase bcc region suitable for homogenisation heat treatments. Predictions for the equimolar TiVCrNb composition (Fig. 1a) show a complex temperature-dependent phase evolution, consistent with prior studies.[14,23] At low temperatures (25–500 °C), a multiphase mixture of hcp, C15 Laves, and two bcc phases (bcc and bcc#2) is predicted. Above ≈500 °C, the hcp phase becomes unstable, leaving a Ti- and Nb-rich primary bcc phase as the major constituent (>60 mol%), accompanied by a Cr-rich C15 Laves phase of the type $Nb_{1-x}(Ti,V)_xCr_2$ and a Ti/Nb-deficient secondary bcc phase (≈20 mol% each). The two bcc phases merge into a single phase above ≈700 °C, while the Laves phase remains stable up to ≈900 °C, resulting in a single-phase bcc region between ≈900 °C and the liquidus (≈1600 °C).

To extend the single-phase bcc stability to lower temperatures, off-equimolar compositions were explored by decreasing Nb while increasing Ti and V. Alloys of the form $Ti_{30+x}V_{30+x}Cr_{24}Nb_{16-2x}$ ($x = 0$, 1, 2) were examined (Fig. S1a–c); the rationale is detailed in the Experimental section. Reducing the Nb content destabilised the C15 Laves phase, suppressing it to approximately the same stability range as the secondary bcc phase (bcc#2) at 16 at% Nb ($x = 0$). This predicts a single-phase bcc region extending from ≈700 °C to the liquidus (Fig. 1b). While further Nb reduction ($x = 1$, 2) decreased the C15 stability range, it did not significantly lower the bcc#2 solvus temperature. Consequently, as reducing Nb further did not broaden the single-phase region, $Ti_{30}V_{30}Cr_{24}Nb_{16}$ was selected for synthesis and further investigation.

3.2 Dendrite suppression *via* increased cooling rate

Based on the CALPHAD predictions, the $Ti_{30}V_{30}Cr_{24}Nb_{16}$ alloy was synthesised using three solidification techniques – arc-melting, suction casting, and melt spinning – to produce both dendritic as-cast samples and dendrite-free counterparts through rapid solidification. These methods span a wide range of cooling rates, from approximately 10^2–10^3 Ks^{-1} for arc-melting and suction casting (with suction casting approximately twice as fast as arc-melting) to ≈10^5 Ks^{-1} for melt spinning.[35,36] All three routes yielded a single bcc phase (space group $Im\bar{3}m$) with comparable lattice parameters a of 3.12 Å, 3.12 Å, and 3.11 Å for the arc-melted, suction cast, and melt-spun samples, respectively (Fig. 2g; details on the Pawley fits, including unit-cell parameter errors, are given in Table S1).

At the lowest cooling rate, arc-melted samples solidified with coarse columnar grains ≈200 μm wide, and Nb/V-rich dendritic regions approximately 30 μm thick (Fig. 2a, b and Table 1). EDS analysis (Table 1 and Fig. S2) revealed co-segregation of Nb and V within the dendrites, and enrichment of Ti and Cr in the interdendritic regions, with compositional variations of 3–5 at% for each element. Increasing the cooling rate through suction casting produced finer columnar grains (≈50 μm wide) and narrower dendrites (≈15 μm) while retaining similar segregation trends (Fig. 2c, d and S2). Elemental variations were on a similar level to arc melting (4–6 at%, Table 1), indicating that microsegregation persisted despite faster solidification.

The highest cooling rate, achieved by melt spinning, produced a distinctly different microstructure. The ribbons exhibited a mixed grain morphology consisting of elongated and spherical grains 2–4 μm in diameter, with no dendritic features visible on the micron level (Fig. 2e and f). EDS mapping

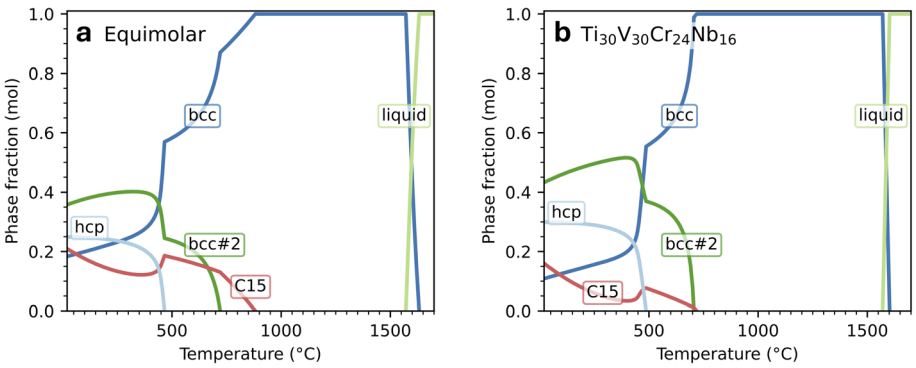

Fig. 1 CALPHAD predicted phase fractions as a function of temperature for (a) equimolar TiVCrNb and (b) $Ti_{30}V_{30}Cr_{24}Nb_{16}$, which was selected for synthesis.

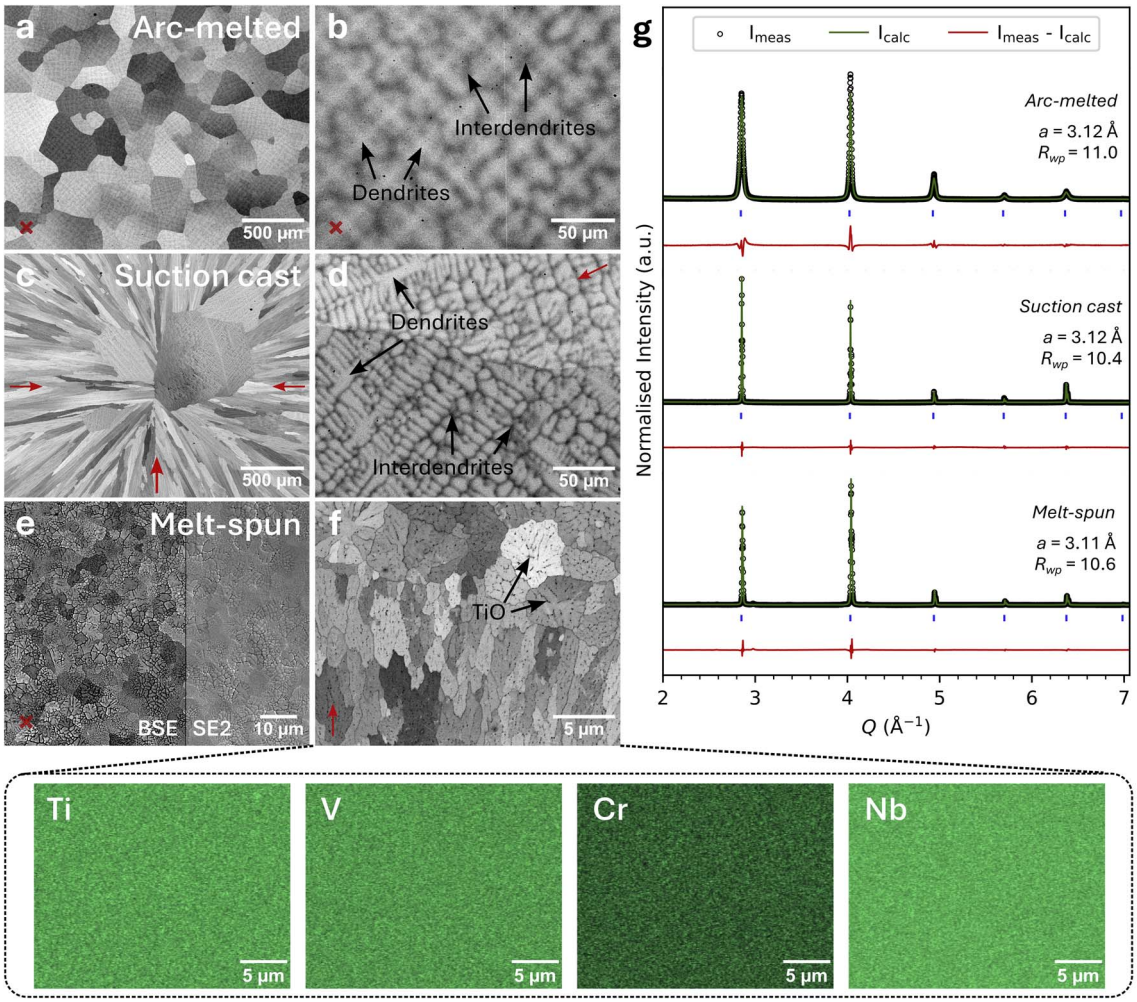

Fig. 2 Microstructure (SEM-BSE) and phase identification of $Ti_{30}V_{30}Cr_{24}Nb_{16}$ alloys produced by (a andb) arc melting, (c and d) suction casting, and (e and f) melt spinning, with EDS maps corresponding to (f). Red arrows and × denote the solidification direction, with × indicating solidification towards the viewer. All images show cross-sections except for (e), which shows the surface of the melt-spun ribbon, imaged by BSE and SE detectors. (g) XRD patterns with Pawley refinements and refined lattice parameters; tick marks indicate reflections from a bcc solid solution ($Im\bar{3}m$).

(Fig. 2f) confirmed a uniform elemental distribution of the metallic constituents, indicating chemical homogeneity consistent with a dendrite-free microstructure. However, fine features smaller than 1 μm were observed on both the surface (Fig. 2e) and cross-section (Fig. 2f) of the ribbons. While their composition could not be resolved by EDS due to the spatial resolution limit (1–2μm), the contrast observed in SEM suggests that they correspond either to pores or to a secondary phase of substantially lower electron density than the matrix. As shown in Section 3.5, neutron diffraction analysis later identified a <2 wt% fraction of the high-temperature TiO phase, suggesting that these features may correspond to a TiO- or (Ti, V, Cr, Nb)O-type oxide formed during solidification.

3.3 Dendrite removal *via* annealing

To complement the rapid solidification approach described in Section 3.2, dendrite-free microstructures were also obtained through post-solidification homogenisation. Suction-cast $Ti_{30}V_{30}Cr_{24}Nb_{16}$ samples, which exhibited moderate dendritic segregation, were annealed at 1000 °C and 1400 °C, both within the single-phase bcc stability range predicted by CALPHAD (Section 3.1). These treatments aimed to eliminate elemental segregation through solid-state diffusion while avoiding secondary phase formation.

Despite the predicted single-phase stability above ≈700 °C, annealing at 1000 °C for 14 days led to the formation of a C15 Laves phase (space group $Fd\bar{3}m$). SEM imaging (Fig. 3c) revealed inter- and intragranular precipitates distributed within an otherwise homogeneous matrix. EDS analysis (Table 2 and Fig. S3) showed that the matrix had an average composition of $Ti_{37}V_{33}Cr_{16}Nb_{14}$, whereas the precipitates were enriched in Nb and Cr, with an average composition of $Ti_{15}V_{25}Cr_{40}Nb_{19}$. These results suggest that the precipitates correspond to the Laves phase observed by XRD (Fig. 3a), with AB_2 stoichiometry $(Ti_{0.26}V_{0.42}Nb_{0.32})Cr_2$, while the surrounding bcc matrix was correspondingly enriched in Ti and depleted in Cr. The

Table 1 Elemental compositions (at%) of $Ti_{30}V_{30}Cr_{24}Nb_{16}$ alloys produced by arc melting, suction casting, and melt spinning, obtained from EDS analyses. Values are given for the nominal composition, area-averaged EDS maps, and, where applicable, dendritic and interdendritic regions. Dendritic and interdendritic compositions are based on five point analyses each, reported as mean values with standard deviations in parentheses

Sample	Region	Ti	V	Cr	Nb
Arc-melted	Nominal	30	30	24	16
	Average (map sum)	30.2	30.3	24.3	15.3
	Dendritic (D)	28.3(1)	32.1(2)	22.9(3)	16.7(1)
	Interdendritic (ID)	33.1(7)	27.7(6)	25.8(3)	13.4(3)
	Difference (D-ID)	−4.8	4.4	−2.9	3.3
Suction cast	Nominal	30	30	24	16
	Average (map sum)	29.9	30.1	23.9	16.0
	Dendritic (D)	28.0(2)	32.2(4)	22.2(3)	17.6(1)
	Interdendritic (ID)	33.7(13)	26.3(13)	26.9(8)	13.1(8)
	Difference (D-ID)	−5.7	5.9	−4.7	4.5
Melt spun	Nominal	30	30	24	16
	Average (map sum)	29.9	30.0	24.0	16.2

emergence of a Laves phase at this intermediate temperature is consistent with previous reports on MPEAs,[16,18,37] and studies of similar alloy systems have likewise shown that the TCHEA3 database tends to underestimate the stabilities of intermetallic phases.[38,39] In view of previous reports of complete homogenisation of comparable alloys at 1400 °C,[15,16] a separate sample was therefore annealed at this temperature.

Annealing at 1400 °C for 1 hour produced a fully single-phase bcc structure, free from both dendrites and secondary precipitates. XRD (Fig. 3a) revealed a single dominant bcc reflection associated with strong texture, indicative of a near-single-crystal morphology resulting from abnormal grain growth during the annealing, which was confirmed by SEM (Fig. S4). SEM and EDS mapping (Fig. 3d and S3) showed uniform elemental distribution across the sample, confirming complete microstructural homogenisation of $Ti_{30}V_{30}Cr_{24}Nb_{16}$ without secondary phase formation. This fully homogenised condition was subsequently used to evaluate the effect of dendrite removal on hydrogen absorption thermodynamics (Section 3.4).

3.4 Microstructural influence on hydrogen absorption behaviour

With dendritic and dendrite-free samples established, the influence of dendritic segregation on the thermodynamics of hydrogen absorption was examined to determine the extent to which compositional variations affect the hydride formation in this MPEA. Hydrogen absorption measurements were performed on the dendritic as-cast and the dendrite-free homogenised (annealed) suction-cast samples. Pressure-composition isotherms (PCIs) were recorded at 105 °C, 130 °C, and 155 °C, and the corresponding equilibrium plateau pressures, plateau slopes, and thermodynamic parameters (ΔH and ΔS) for dihydride formation were determined to quantify potential microstructure-dependent differences. The dendrite-free melt-spun sample was excluded from comparison as it did not absorb hydrogen under the present conditions, even after two days of exposure. This inhibited absorption could potentially be due to <2 wt% of a finely dispersed oxide within the grains (Sections 3.2 and 3.5) that hinders hydrogen uptake by raising the equilibrium pressure for hydride formation,[40] or other microstructural differences, and is further discussed in Section 4. Absorption may still occur at higher pressures, but with altered thermodynamics and kinetics,[40,42] precluding a meaningful comparison with the suction-cast alloys.

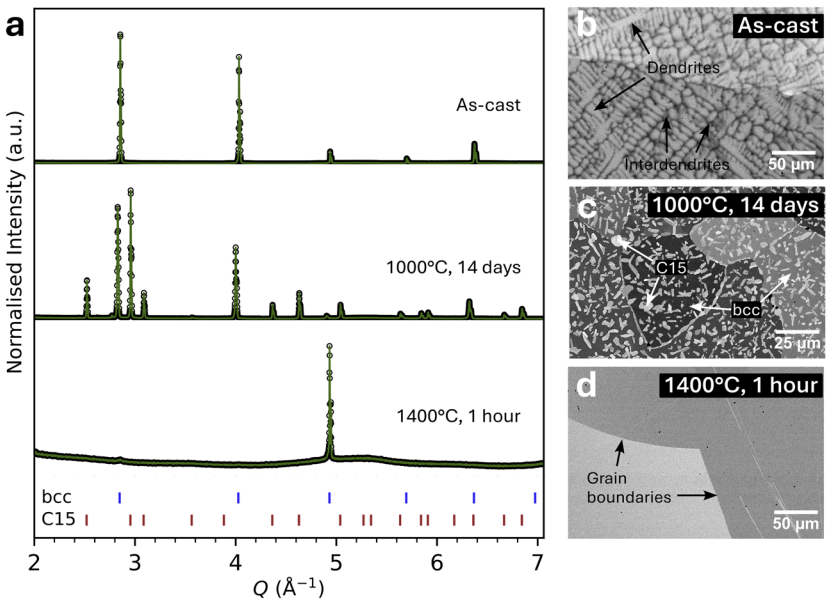

Fig. 3 (a) XRD patterns of suction-cast $Ti_{30}V_{30}Cr_{24}Nb_{16}$ alloys in the as-cast state and after annealing at 1000 °C for 14 days and 1400 °C for 1 h. Tick marks indicate reflections from a bcc solid solution (blue) and a Laves C15 phase (red). (b–d) Corresponding microstructures (SEM-BSE).

Table 2 Elemental compositions (at%) of suction-cast $Ti_{30}V_{30}Cr_{24}Nb_{16}$ alloys annealed at 1000 °C and 1400 °C, obtained from EDS analyses. Values are given for the nominal composition, area-averaged EDS maps, and, where applicable, individual phases. Phase compositions are based on five point analyses each, reported as mean values with standard deviations in parentheses

Treatment	Region	Ti	V	Cr	Nb
1000 °C, 14 days	Nominal	30	30	24	16
	Average (map sum)	30.2	30.2	23.7	15.9
	BCC phase	37.0(3)	32.6(3)	16.1(3)	14.3(2)
	C15 phase	15.3(2)	25.3(1)	40.3(2)	19.1(2)
1400 °C, 1h	Nominal	30	30	24	16
	Average (map sum)	30.0	30.0	24.0	16.0

Both the dendritic and dendrite-free suction cast samples exhibited rapid hydrogen uptake during activation, reaching a maximum capacity of 1.96 H/M (3.3 wt%) upon exposure to 54 bar H_2 at 25 °C (Fig. S5). As typical for bcc-structured metals and alloys, hydride formation proceeded through a two-step phase transition from the solid solution to a near-monohydride (MH_{1-x}) and subsequently to a dihydride (MH_{2-x}).[6,7] This is evident in the PCIs (Fig. 4a) as an initial absorption up to 0.8 H/M, followed by a rapid rise in equilibrium pressure and the appearance of a second plateau extending from approximately $MH_{0.85}$ to MH_{2-x} (exact composition depending on temperature). As the equilibrium pressure of the first transition (alloy → monohydride) was below the pressure-sensor detection limit at all temperatures, only the second plateau, corresponding to the monohydride-dihydride transition, is presented in Fig. 4 and b and used for the thermodynamic analysis.

At a hydrogen concentration of 1.1 H/M, the equilibrium plateau pressures for the monohydride-dihydride transition were 1.44, 4.38, and 10.99 bar for the dendritic sample, and 1.51, 4.70, and 11.40 bar for the homogenised sample at 105 °C, 130 °C, and 155 °C, respectively. Across all conditions, the plateau displayed a linear pressure-composition region, transitioning into an exponential increase at higher hydrogen concentrations due to H–H repulsion.[43] Linear fitting of the central plateau region (Fig. 4b) revealed a systematic temperature-dependent difference in the plateau slope $\frac{dP_{eq}}{dx}$, where x is the H-concentration in H/M, between the samples. As shown in Fig. 4c, the plateau slope increased exponentially with temperature for both samples, but remained consistently lower in the homogenised sample. The slope of the homogenised sample was 0.26(6), 1.35(11), and 1.91(38) bar per H/M lower than that of the dendritic sample at 105 °C, 130 °C, and 155 °C, respectively. This confirms that reduced elemental (dendritic) segregation flattens but does not eliminate the slope, and indicates that dendritic alloys have a broader distribution of local chemical environments surrounding interstitial hydrogen compared to homogenised MPEAs.

Despite these differences in plateau slope, van't Hoff analysis (Fig. 4d and S6) revealed no statistically significant differences in the thermodynamic parameters of the monohydride-dihydride transition. Using equilibrium pressures at 1.1 H/M, the enthalpy and entropy changes were determined as $\Delta H = -54.8 \pm 1.1$ kJ mol^{-1} H_2 and $\Delta S = -148.1 \pm 2.7$ J mol^{-1} H_2·K for the dendritic sample, and $\Delta H = -54.5 \pm 1.9$ kJ mol^{-1} H_2 and $\Delta S = -147.6 \pm 4.8$ J mol^{-1} H_2·K for the homogenised sample, where the uncertainty represents the linear fit error. These values also overlap within the fitting uncertainty for all extraction points (H/M = 0.9, 1.1, or 1.3) (Fig. S6). The results, therefore, indicate that, while homogenisation reduces plateau sloping and improves absorption uniformity, ΔH and ΔS are unaffected by dendritic microstructures in this alloy.

3.5 Oxide quantification in dendrite-free alloys

Neutron diffraction was used to determine whether oxide formation accounted for the lack of hydrogen absorption in the dendrite-free melt-spun sample, in contrast to the dendrite-free suction-cast alloy. Owing to the near-zero average coherent scattering length of the alloy relative to oxygen (Section 2.5), this technique provided high sensitivity to even minor oxide phases while probing the bulk of the material.

Both samples exhibited a bcc structure (Fig. 5), with lattice parameters of $a = 3.117(6)$ Å for the suction-cast and 3.113(5) Å for the melt-spun sample (Table S2), consistent with the XRD results. In addition to the bcc reflections, the melt-spun sample showed an additional set of weak peaks, the most intense at 2.6 Å^{-1}, which were indexed to a cubic TiO-type phase (space group $Fm\bar{3}m$) with $a = 4.223(6)$ Å. The refined oxide fraction was below 2 wt%. A weak, unidentified reflection was also observed at 3.1 Å^{-1}.

The oxide lattice parameter was slightly larger than that of stoichiometric TiO (4.19 Å),[44] suggesting either oxygen over-stoichiometry (TiO_{1+x}), or partial substitution of Ti by the other metallic constituents (V, Cr, Nb). Importantly, this TiO-type phase corresponds to the high-temperature cubic TiO (ht2) in the Ti–O system (Fig. S7). Combined with the uniform distribution of oxide throughout the alloy, observed by SEM, and the bulk sensitivity of neutron diffraction, this indicates that the oxide formed during the melt-spinning rather than by post-solidification oxidation. As oxides can hinder hydrogen absorption,[45] the presence of this finely dispersed TiO phase could explain the poor activation behaviour of the melt-spun sample. However, the exact origin in this case is unknown and outside the scope of this work.

4 Discussion

Rapid solidification through melt-spinning effectively suppressed dendritic segregation in $Ti_{30}V_{30}Cr_{24}Nb_{16}$; however, the

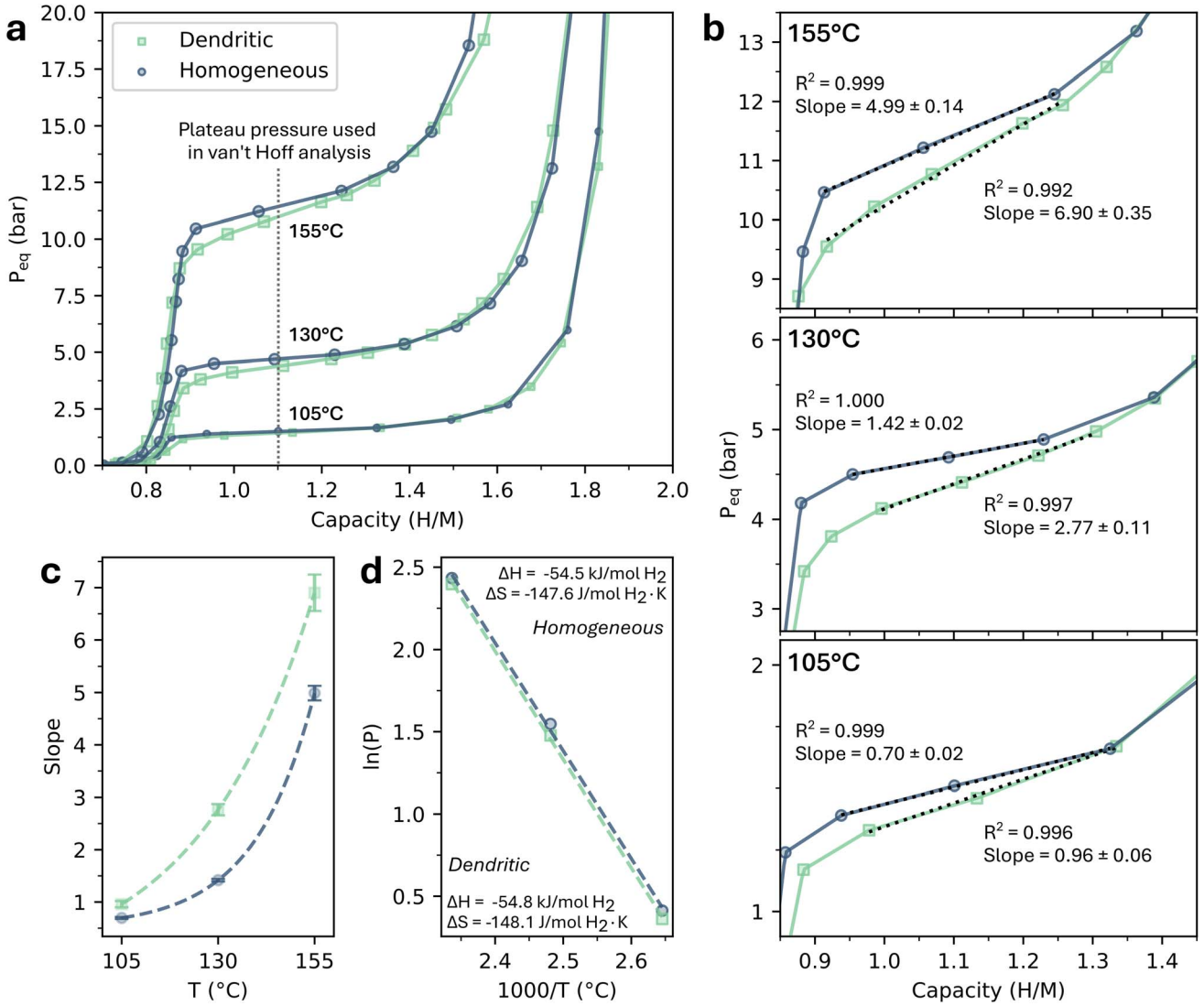

Fig. 4 Hydrogen absorption behaviour of suction-cast $Ti_{30}V_{30}Cr_{24}Nb_{16}$ alloys in the dendritic (as-cast) and homogenised (annealed at 1400 °C) states. (a) Pressure-composition isotherms measured at 105, 130, and 155 °C, showing the second plateau corresponding to the monohydride-dihydride transition. (b) Enlarged views of the plateau regions with linear fits (dotted lines) used to determine the slope; markers denote measured values and solid lines indicate interpolated data. (c) Plateau slope as a function of temperature for each sample, with an exponential trendline shown as a visual guide. Error bars represent the standard error of the linear fits in (b). (d) van't Hoff plot constructed from equilibrium pressures at 1.1 H/M, with corresponding linear fit equations and calculated hydride formation enthalpy (ΔH) and entropy (ΔS).

resulting ribbons exhibited poor activation behaviour, with no measurable hydrogen uptake after activation at 410 °C for 3 h followed by 48 h exposure to 54 bar H_2 at 25 °C. In contrast, the suction cast alloy absorbed 3.3 wt% hydrogen within 2 min under the same conditions and identical activation. Similar activation difficulties have been reported by Yu *et al.*[41] for melt-spun $Ti_{47}V_{28}Mn_{15}Cr_{10}$ alloys and were speculated to originate from the formation of titanium-based surface oxides after solidification. Our results reveal <2 wt% of a high-temperature-stable TiO-type oxide phase that likely formed during solidification rather than by post-solidification oxidation, as supported by neutron diffraction and the uniformly dispersed oxide observed in SEM. The presence of oxides can increase the equilibrium plateau pressure and hinder hydrogen diffusion,[40,42] potentially explaining the lack of absorption. However, non-stoichiometric TiO_x has also been shown to absorb hydrogen at relatively low pressures,[46] suggesting that the lack of absorption may originate from other microstructural differences. Further studies are needed to definitively determine the origin of the activation difference between the melt-spun and cast samples, and what role the TiO_x has in the absorption. Nevertheless, these findings indicate that while melt spinning suppresses dendritic segregation, other structural differences do impede activation.

Solid-solution annealing at 1400 °C homogenised the alloy by eliminating dendritic segregation without forming secondary phases, leading to reductions in the plateau slope of 0.26(6), 1.35(11), and 1.91(38) bar per H/M at 105 °C, 130 °C,

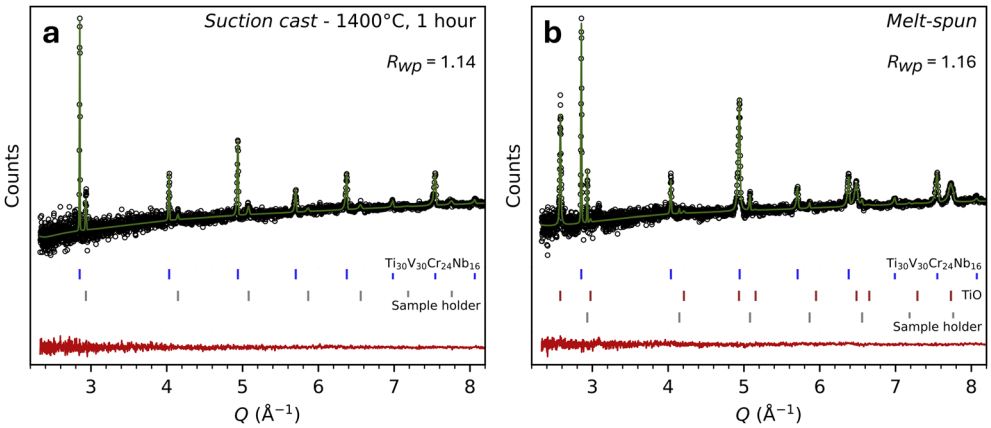

Fig. 5 Neutron diffraction patterns (black circles) of $Ti_{30}V_{30}Cr_{24}Nb_{16}$ alloys produced by (a) suction casting followed by homogenisation at 1400 °C for 1 h and (b) melt-spinning, with corresponding Rietveld fits (green lines) and difference curves (red lines). Tick marks indicate reflections from the main bcc solid solution phase (blue), sample holder (V-can, grey), and TiO (red).

and 155 °C, respectively, for the monohydride-dihydride transition. This flattening agrees with previous reports[11–13] and is primarily attributed to the removal of micro-level elemental segregation associated with dendritic microstructures, which reduces the variation in local chemical potential of the interstitial sites. Additional contributions may arise from strain relief and reduced grain boundary density, as the annealed microstructure exhibited extreme grain growth. Both effects would narrow the range of local site energies by relaxing internal stresses and decreasing boundary-related heterogeneities.

Nevertheless, the plateau did not become fully flat, indicating that residual variations in interstitial site energies persist even after homogenisation, consistent with previous observations.[11–13] This residual sloping likely originates from atomic-scale chemical and structural heterogeneities inherent to MPEAs. Even in a perfectly random solid solution, hydrogen occupies interstitial sites surrounded by diverse nearest-neighbour configurations (*e.g.*, Ti–Ti–Ti–Ti, Ti–Ti–V–Cr, Ti–V–Cr–Nb), each associated with different site energies. Even sites with identical nearest-neighbour combinations may also differ in energy due to next-nearest-neighbour interactions and local structural distortions. Additional broadening of the energy distribution arises from grain boundaries and structural defects. For example, vacancies have been shown to alter the preferred hydrogen site occupancy from tetrahedral to octahedral positions,[47] further diversifying local chemical potentials.

Despite differences in plateau slope with microstructure, the derived thermodynamic parameters (ΔH and ΔS) for the monohydride-to-dihydride formation were indistinguishable within experimental uncertainty. Moreover, these values were insensitive to the point along the plateau used for the van't Hoff analysis, indicating that microstructural homogenisation and plateau sloping do not significantly influence the intrinsic thermodynamics of hydride formation in $Ti_{30}V_{30}Cr_{24}Nb_{16}$. However, it is apparent that the difference in sloping between the homogenised and dendritic samples increases with temperature, suggesting that van't Hoff analyses conducted at higher temperatures may result in more pronounced differences. As most van't Hoff analyses for bcc alloys are performed around the temperature range investigated here, the negligible variation between microstructures provides important validation for existing machine-learning models[10] trained on thermodynamic data from as-cast dendritic alloys. Nevertheless, similar studies on other bcc alloy systems are encouraged to assess the generality of this observation.

This contrasts with the findings of Rong *et al.*,[11] who reported a 4% difference in ΔH (-29.84 ± 0.14 *vs.* -28.68 ± 0.12 kJ mol^{-1} H_2) between as-cast and annealed $Ti_{20}V_{68}Cr_{12}$ alloys. A similar dependence is also evident in the work of Shilov and Efremenko[12] on $LaNi_{4.7}Al_{0.3}$. To enable comparison with the present study, van't Hoff analysis was performed here using the equilibrium pressures reported in their study. This yielded $\Delta H = -33.0 \pm 1.3$ kJ mol^{-1} H_2 and $\Delta S = -104.0 \pm 3.3$ J mol^{-1} $H_2 \cdot K$ for the as-cast sample, compared with $\Delta H = -36.5 \pm 0.2$ kJ mol^{-1} H_2 and $\Delta S = -115.2 \pm 0.4$ J mol^{-1} $H_2 \cdot K$ for the annealed sample, using pressures extracted near the monohydride end of the plateau. When pressures were instead taken from the dihydride end of the plateau, ΔH and ΔS decreased to -29.2 ± 0.7 kJ mol^{-1} H_2 and -99.9 ± 1.8 J mol^{-1} $H_2 \cdot K$ for the as-cast alloy, and -34.5 ± 0.8 kJ mol^{-1} H_2 and -112.6 ± 2.0 J mol^{-1} $H_2 \cdot K$ for the annealed alloy. These variations between samples and along the plateau are consistent with the microstructure-dependent thermodynamics proposed by Rong *et al.*[11]

The divergence between these studies and the present work may stem from differences in alloy composition or measurement methodology. In both Rong *et al.*[11] and Shilov and Efremenko's[12] analyses, plateau pressures were extracted at varying hydrogen concentrations across samples and temperatures, potentially introducing shifts in ΔH and ΔS due to the composition dependence of the equilibrium pressure. In contrast, our van't Hoff analyses used pressures determined at consistent H/M ratios across all samples and temperatures, reducing the source of variability. Whether the discrepancies originate from compositional effects or from differences in how plateau

pressures are defined remains an open question requiring further study.

5 Conclusion

This study examined the influence of dendritic microstructures on the thermodynamic parameters (ΔH and ΔS) of hydride formation in the MPEA $Ti_{30}V_{30}Cr_{24}Nb_{16}$. Dendrite suppression and removal were achieved through rapid solidification by melt-spinning and high-temperature homogenisation, respectively, without the formation of secondary intermetallic phases. While both techniques successfully removed dendrites, melt-spinning resulted in the formation of <2 wt% of a finely dispersed TiO-type oxide and an alloy that did not absorb hydrogen. These findings indicate that dendrite removal through heat treatment potentially is a more suitable processing route for Ti-based alloys for hydrogen storage applications than dendrite suppression *via* melt-spinning.

Comparing the as-cast and annealed suction cast alloys revealed that, despite differences in microstructure and plateau slope, the derived thermodynamic parameters (ΔH and ΔS) for the monohydride-dihydride transition were indistinguishable within experimental uncertainty. This demonstrates that the thermodynamics of this system are insensitive to the compositional fluctuations observed. While homogenisation remains advantageous for applications due to a flatter plateau and more uniform hydrogen absorption, reliable thermodynamic data can in this case evidently be obtained from as-cast dendritic MPEAs.

This has important implications for data-driven materials discovery, since ML models for metal hydrides overwhelmingly rely on training databases constructed from as-cast alloys. Although the generality of this microstructure independence remains to be established through studies on other alloy systems, the present work demonstrates that intrinsic thermodynamic parameters remain robust despite segregation in a representative system. As such, these results provide important validation for the use of as-cast data in high-throughput alloy screening.

Author contributions

Veronica Enblom: conceptualisation, methodology, investigation, data curation, writing – original draft, writing – review & editing, visualisation. Fernando Maccari: investigation, writing – review & editing. Franziska Scheibel: investigation, writing – review & editing. Aaron Keith: investigation, writing – review & editing. Vitalie Stavila: supervision, writing – review & editing. Claudia Zlotea: formal analysis, resources, writing – review & editing. Oliver Gutfleisch: resources, writing – review & editing. Paul F. Henry: formal analysis, writing – review & editing, supervision. Martin Sahlberg: conceptualisation, resources, writing – review & editing, supervision, funding acquisition.

Conflicts of interest

There are no conflicts to declare.

Data availability

Neutron diffraction data for this article are available at ISIS Neutron and Muon Source Data Journal at https://doi.org/10.5286/ISIS.E.RB2590128-1 and https://doi.org/10.5286/ISIS.E.RB2590129-1.

Supplementary information (SI): further characterisation details. See DOI: https://doi.org/10.1039/d5ta10141g.

Acknowledgements

VE and MS gratefully acknowledge funding from ÅForsk (grant 22-29) and the Olle Engkvist Foundation (grant 218-0055). VE additionally acknowledges support from the Axel Hultgren Foundation for funding participation in the 2025 Gordon Research Conference on Hydrogen-Metal Systems, where part of this work was presented, and the Science and Technology Facilities Council (STFC) for the provision of neutron beamtime at POLARIS, ISIS (RB2590128 and RB2590129). Special thanks to Andrei Agafonov for guidance on kinetics and PCI measurements. FS and OG acknowledge funding from the Deutsche Forschungsgemeinschaft (DFG) CRC/TRR 270 "HoMMage" (Project-ID 405553726-TRR 270), MS acknowledges a Mercator fellowship within CRC/TRR 270 "HoMMage". VS gratefully acknowledges research support from the Department of Energy's National Nuclear Security Administration (NNSA) under the Trilateral Framework on Cooperation in Science and Innovation among the NNSA, the Cabinet Office of Japan, and the Ministry of Science and ICT of the Republic of Korea. Sandia National Laboratories is a multi-mission laboratory managed and operated by National Technology and Engineering Solutions of Sandia, LLC., a wholly owned subsidiary of Honeywell International, Inc., for the U.S. Department of Energy's National Nuclear Security Administration (NNSA) under contract DE-NA-0003525.

References

1 Hydrogen Storage, https://www.energy.gov/eere/fuelcells/hydrogen-storage, accessed 16 January 2024.
2 F. Marques, M. Balcerzak, F. Winkelmann, G. Zepon and M. Felderhoff, Review and outlook on high-entropy alloys for hydrogen storage, *Energy Environ. Sci.*, 2021, **14**, 5191–5227.
3 Y. T. Zhai, Y. M. Li, S. H. Wei, I. Tolj, J. Kennedy and F. Yang, Progress in V-BCC based solid solution hydrogen storage alloys, *J. Energy Storage*, 2025, **109**, 115103.
4 J.-M. Joubert, V. Paul-Boncour, F. Cuevas, J. Zhang and M. Latroche, LaNi5 related AB5 compounds: Structure, properties and applications, *J. Alloys Compd.*, 2021, **862**, 158163.
5 V. A. Yartys, M. V. Lototskyy, E. Akiba, R. Albert, V. E. Antonov, J. R. Ares, M. Baricco, N. Bourgeois, C. E. Buckley, J. M. Bellosta von Colbe, J.-C. Crivello, F. Cuevas, R. V. Denys, M. Dornheim, M. Felderhoff, D. M. Grant, B. C. Hauback, T. D. Humphries, I. Jacob, T. R. Jensen, P. E. de Jongh, J.-M. Joubert,

M. A. Kuzovnikov, M. Latroche, M. Paskevicius, L. Pasquini, L. Popilevsky, V. M. Skripnyuk, E. Rabkin, M. V. Sofianos, A. Stuart, G. Walker, H. Wang, C. J. Webb and M. Zhu, Magnesium based materials for hydrogen based energy storage: Past, present and future, *Int. J. Hydrogen Energy*, 2019, **44**, 7809–7859.

6 T. Schober and H. Wenzl, in *Hydrogen in Metals II*, ed G. Alefeld and J. Völkl, Springer Berlin Heidelberg, Berlin, Heidelberg, 1978, vol. 29, pp. 11–71.

7 F. Greaves, A. Bouzidi, L. Perrière, G. Vaughan, V. Nassif, L. Laversenne, A. Borgschulte, M. L. Martins, Y. Cheng, A. J. Ramirez-Cuesta, P. Á. Szilágyi, P. Cullen and C. Zlotea, Hydrogen Induced Phase Transition in TiZrNbHfV1–xTax High Entropy Alloys, *J. Phys. Chem. C*, 2025, **129**, 2904–2912.

8 M. Hirabayashi and H. Asano, in *Metal Hydrides*, ed. G. Bambakidis, Springer US, Boston, MA, 1981, pp. 53–80.

9 D. G. Westlake, in *Metal Hydrides*, ed. G. Bambakidis, Springer US, Boston, MA, 1981, pp. 145–176.

10 M. D. Witman, S. Ling, M. Wadge, A. Bouzidi, N. Pineda-Romero, R. Clulow, G. Ek, J. M. Chames, E. J. Allendorf, S. Agarwal, M. D. Allendorf, G. S. Walker, D. M. Grant, M. Sahlberg, C. Zlotea and V. Stavila, Towards Pareto optimal high entropy hydrides *via* data-driven materials discovery, *J. Mater. Chem. A*, 2023, **11**, 15878–15888.

11 M. Rong, F. Wang, J. Wang, Z. Wang and H. Zhou, Effect of heat treatment on hydrogen storage properties and thermal stability of V68Ti20Cr12 alloy, *Prog. Nat. Sci. Mater. Int.*, 2017, **27**, 543–549.

12 A. L. Shilov and N. E. Efremenko, Effect of sloping pressure 'plateau' in two-phase regions of hydride systems, *Russ. J. Phys. Chem.*, 1986, **60**, 3024–3028.

13 M. V. Lototsky, V. A. Yartys and I. Yu. Zavaliy, Vanadium-based BCC alloys: phase-structural characteristics and hydrogen sorption properties, *J. Alloys Compd.*, 2005, **404–406**, 421–426.

14 R. B. Strozi, B. H. Silva, D. R. Leiva, C. Zlotea, W. J. Botta and G. Zepon, Tuning the hydrogen storage properties of Ti-V-Nb-Cr alloys by controlling the Cr/(TiVNb) ratio, *J. Alloys Compd.*, 2023, **932**, 167609.

15 O. N. Senkov, D. B. Miracle, K. J. Chaput and J.-P. Couzinie, Development and exploration of refractory high entropy alloys—A review, *J. Mater. Res.*, 2018, **33**, 3092–3128.

16 R. Feng, B. Feng, M. C. Gao, C. Zhang, J. C. Neuefeind, J. D. Poplawsky, Y. Ren, K. An, M. Widom and P. K. Liaw, Superior High-Temperature Strength in a Supersaturated Refractory High-Entropy Alloy, *Adv. Mater.*, 2021, **33**, 2102401.

17 J. Liu, R. J. Scales, B.-S. Li, M. Goode, B. A. Young, J. Hu, A. J. Wilkinson and D. E. J. Armstrong, Controlling microstructure and mechanical properties of Ti-V-Cr-Nb-Ta refractory high entropy alloys through heat treatments, *J. Alloys Compd.*, 2023, **932**, 167651.

18 D. B. Miracle and O. N. Senkov, A critical review of high entropy alloys and related concepts, *Acta Mater.*, 2017, **122**, 448–511.

19 G. Gottstein, *Physical Foundations of Materials Science*, Springer Berlin/Heidelberg, Berlin, Heidelberg, Germany, 2004.

20 M. M. Nygård, G. Ek, D. Karlsson, M. H. Sørby, M. Sahlberg and B. C. Hauback, Counting electrons - A new approach to tailor the hydrogen sorption properties of high-entropy alloys, *Acta Mater.*, 2019, **175**, 121–129.

21 B. Cheng, Y. Li, X. Li, H. Ke, L. Wang, T. Cao, D. Wan, B. Wang and Y. Xue, Solid-State Hydrogen Storage Properties of Ti–V–Nb–Cr High-Entropy Alloys and the Associated Effects of Transitional Metals (M = Mn, Fe, Ni), *Acta Metall. Sin.*, 2023, **36**, 1113–1122.

22 B. Hessel Silva, W. J. Botta and G. Zepon, Design of a Ti–V–Nb–Cr alloy with room temperature hydrogen absorption/desorption reversibility, *Int. J. Hydrogen Energy*, 2023, **48**, 32813–32825.

23 R. B. Strozi, D. R. Leiva, G. Zepon, W. J. Botta and J. Huot, Effects of the Chromium Content in (TiVNb)100−xCrx Body-Centered Cubic High Entropy Alloys Designed for Hydrogen Storage Applications, *Energies*, 2021, **14**, 3068.

24 M. M. Nygård, Ø. S. Fjellvåg, M. H. Sørby, K. Sakaki, K. Ikeda, J. Armstrong, P. Vajeeston, W. A. Sławiński, H. Kim, A. Machida, Y. Nakamura and B. C. Hauback, The average and local structure of TiVCrNbDx (x=0,2.2,8) from total scattering and neutron spectroscopy, *Acta Mater.*, 2021, **205**, 116496.

25 B. H. Silva, C. Zlotea, G. Vaughan, Y. Champion, W. J. Botta and G. Zepon, Hydrogen absorption/desorption reactions of the (TiVNb)85Cr15 multicomponent alloy, *J. Alloys Compd.*, 2022, **901**, 163620.

26 Y. Zhu, X. Li, X.-S. Yang, P. Chen, G. C.-P. Tsui, Z.-L. Xu, R. Tang, F. Xiao and K. Chan, Compositionally complex doping for low-V Ti-Cr-V hydrogen storage alloys, *Chem. Eng. J.*, 2023, **477**, 146970.

27 N. Y. Yurchenko, E. S. Panina, S. V. Zherebtsov, M. A. Tikhonovsky, G. A. Salishchev and N. D. Stepanov, Microstructure evolution of a novel low-density Ti–Cr–Nb–V refractory high entropy alloy during cold rolling and subsequent annealing, *Mater. Charact.*, 2019, **158**, 109980.

28 J.-O. Andersson, T. Helander, L. Höglund, P. Shi and B. Sundman, Thermo-Calc & DICTRA, computational tools for materials science, *Calphad*, 2002, **26**, 273–312.

29 J. P. Couzinié, G. Dirras, L. Perrière, T. Chauveau, E. Leroy, Y. Champion and I. Guillot, Microstructure of a near-equimolar refractory high-entropy alloy, *Mater. Lett.*, 2014, **126**, 285–287.

30 R. I. Smith, S. Hull, M. G. Tucker, H. Y. Playford, D. J. McPhail, S. P. Waller and S. T. Norberg, The upgraded Polaris powder diffractometer at the ISIS neutron source, *Rev. Sci. Instrum.*, 2019, **90**, 115101.

31 V. Enblom, P. F. Henry, Investigating the influence of sample preparation routes on the diffuse scattering in a refractory HEA: Sample 2, STFC ISIS Neutron and Muon Source, 2025, DOI: 10.5286/ISIS.E.RB2590128-1.

32 V. EnblomP. F. Henry, Investigating the influence of sample preparation routes on the diffuse scattering in a refractory

HEA: Sample 3, STFC ISIS Neutron and Muon Source, 2025, DOI: 10.5286/ISIS.E.RB2590128-1.
33 A. A. Coelho, TOPAS and TOPAS-Academic: an optimization program integrating computer algebra and crystallographic objects written in C++, *J. Appl. Crystallogr.*, 2018, **51**, 210–218.
34 K. J. Gross, K. R. Carrington, S. Barcelo, A. Karkamkar, J. Purewal, S. Ma, H.-C. Zhou, P. Dantzer, K. Ott, T. Burrell, T. Semeslberger, Y. Pivak, B. Dam, D. Chandra and P. Parilla, *Recommended Best Practices for the Characterization of Storage Properties of Hydrogen Storage Materials*, U.S. D.O.E. Hydrogen Program, 2012.
35 V. I. Tkatch, A. I. Limanovskii, S. N. Denisenko and S. G. Rassolov, The effect of the melt-spinning processing parameters on the rate of cooling, *Mater. Sci. Eng., A*, 2002, **323**, 91–96.
36 T. Kozieł, Estimation Of Cooling Rates In Suction Casting And Copper-Mould Casting Processes, *Arch. Metall. Mater.*, 2015, **60**, 767–771.
37 E. P. George, D. Raabe and R. O. Ritchie, High-entropy alloys, *Nat. Rev. Mater.*, 2019, **4**, 515–534.
38 V. Pacheco, G. Lindwall, D. Karlsson, J. Cedervall, S. Fritze, G. Ek, P. Berastegui, M. Sahlberg and U. Jansson, Thermal Stability of the HfNbTiVZr High-Entropy Alloy, *Inorg. Chem.*, 2019, **58**, 811–820.
39 E. S. Panina, N. Y. Yurchenko, S. V. Zherebtsov, M. A. Tikhonovsky, M. V. Mishunin and N. D. Stepanov, Structures and mechanical properties of Ti-Nb-Cr-V-Ni-Al refractory high entropy alloys, *Mater. Sci. Eng., A*, 2020, **786**, 139409.
40 U. Ulmer, K. Asano, T. Bergfeldt, V. S. K. Chakravadhanula, R. Dittmeyer, H. Enoki, C. Kübel, Y. Nakamura, A. Pohl and M. Fichtner, Effect of oxygen on the microstructure and hydrogen storage properties of V–Ti–Cr–Fe quaternary solid solutions, *Int. J. Hydrogen Energy*, 2014, **39**, 20000–20008.
41 X. B. Yu, Z. Wu and N. X. Xu, Effects of melt-quenching rates on the hydrogen storage properties of Ti-based BCC phase alloy, *Phys. B*, 2004, **344**, 456–461.
42 K. Asano, S. Hayashi, K. Mimura, H. Enoki and Y. Nakamura, Effect of dissolved oxygen on hydrogenation of vanadium and hydrogen diffusion in the monohydride phase, *Acta Mater.*, 2016, **103**, 23–29.
43 M. V. Lototsky, V. A. Yartys, V. S. Marinin and N. M. Lototsky, Modelling of phase equilibria in metal–hydrogen systems, *J. Alloys Compd.*, 2003, **356–357**, 27–31.
44 A. V. Skripov, A. V. Soloninin, A. A. Valeeva, A. I. Gusev, A. A. Rempel, H. Wu and T. J. Udovic, Hydrogen in nonstoichiometric cubic titanium monoxides: X-ray and neutron diffraction, neutron vibrational spectroscopy and NMR studies, *J. Alloys Compd.*, 2021, **887**, 161353.
45 M. J. Donachie Jr. and M. J. Donachie, in *Titanium : A Technical Guide*, A S M International, Materials Park, United States, 2000.
46 A. V. Skripov, A. V. Soloninin, A. A. Valeeva, A. I. Gusev, A. A. Rempel, H. Wu and T. J. Udovic, Hydrogen in nonstoichiometric cubic titanium monoxides: X-ray and neutron diffraction, neutron vibrational spectroscopy and NMR studies, *J. Alloys Compd.*, 2021, **887**, 161353.
47 C. M. Moore, J. A. Wilson, M. J. D. Rushton, W. E. Lee, J. O. Astbury and S. C. Middleburgh, Hydrogen accommodation in the TiZrNbHfTa high entropy alloy, *Acta Mater.*, 2022, **229**, 117832.

